

Article

Preparation and Performances of ZIF-67-Derived FeCo Bimetallic Catalysts for CO₂ Hydrogenation to Light Olefins

Zichao Dong ^{1,*†}, Jie Zhao ^{2,†}, Yajie Tian ³, Bofeng Zhang ¹ and Yu Wu ²¹ Key Laboratory for Green Chemical Technology of Ministry of Education, School of Chemical Engineering and Technology, Tianjin University, Tianjin 300350, China; zhangbofeng@tju.edu.cn² SINOPEC Research Institute of Petroleum Process, Beijing 100083, China; zhaojie.ripp@sinopec.com (J.Z.); wuyu.ripp@sinopec.com (Y.W.)³ College of Chemistry and Chemical Engineering, Henan University, Kaifeng 475004, China; yjtian@henu.edu.cn

* Correspondence: dzc08@tju.edu.cn; Tel.: +86-22-8535-6099

† These authors contributed equally to this work.

Received: 5 April 2020; Accepted: 21 April 2020; Published: 23 April 2020



Abstract: A novel sodium-promoted Fe-Co/NC catalyst prepared by incipient-wet-impregnation method using ZIF-67 as a support was employed to convert CO₂ to light olefins through hydrogenation reaction. Properties of the synthesized catalysts calcinated at various temperatures (from 400 to 700 °C) were investigated by XRD, SEM, TEM and Mössbauer spectroscopy. Characterization results showed that the support could be fully converted into carbon support above 500 °C, which could anchor metal particles, thus resulting in a uniform dispersion of active components. Furthermore, the Fe-Co alloy was formed during N₂ calcination, and was converted into active components, such as Fe₃O₄, Fe₅C₂, and Co₂C during the reaction. The reaction result indicated that FeCo/NC-600 catalyst exhibited the highest selectivity of light olefins (C₂= – C₄=, 27%) and CO₂ conversion could reach around 37% when this catalyst pyrolyzed at 600 °C in N₂. The highest selectivity for light olefins may be related to the combination of suitable particle size and sufficient active sites of iron carbide.

Keywords: CO₂ hydrogenation; Co–Fe bimetallic catalyst; N-doped; Mössbauer spectroscopy; ZIF-67; pyrolysis of MOFs

1. Introduction

Due to the global warming concerns and the increasing of ocean acidity, highly efficient capture, and utilization of CO₂ has attracted much attention [1–3]. CO₂ can be used in food additives, oil and gas extraction, and synthesis of chemical material [4], while several high value-added products, such as methane, olefins, liquid fuels, and alcohols can be obtained by CO₂ hydrogenation reaction. Among them, light olefins (C₂= – C₄=) are kinds of indispensable chemicals, and a series of studies have been carried out to research the hydrogenation of CO₂ to light olefins [5–7]. However, adjusting the ratio of different active sites to obtain the best adsorption competition between CO₂ and CO, and obtaining high CO₂ conversion while inhibiting high selectivity of methane and light saturated hydrocarbons are still huge challenges [8].

To our knowledge, Fe-based catalysts have been extensively applied in the CO₂ hydrogenation reaction due to similar characteristics to the traditional Fischer–Tropsch (FT) synthesis process [9–12]. In general, the mechanism of the CO₂ hydrogenation reaction over Fe-based catalysts is based on a revised Fischer–Tropsch path, in which CO is firstly generated by the reverse water gas reaction (RWGS), and then hydrocarbon compounds were generated by the FT reaction [13,14]. Fe₃O₄ and

Fe_5C_2 are generally deemed as the main active sites for each of these two steps [15,16]. However, the single iron-based catalyst has low catalytic activity and is easy to sinter and deposit carbon. To further enhance the CO_2 conversion and improve the selectivity of light olefins, different metal additives and supports were introduced to improve the performance [17,18]. Dossary [19] found that Mn additives can improve the reduction, dispersion, and carbonization of the catalyst by changing the electron density of metal, and enhance the formation of light olefins. Wang [20] found that Cu additives can effectively reduce the reduction temperature of the active phase and promote the production of the active phase, which improved the CO_2 conversion, enhanced the selectivity of CO, and inhibited the generation of methane. While Co additives can effectively reduce the production of carbon deposits and enhance the stability of the catalyst. Besides, alkali metal promoters, such as potassium and sodium, can be used as electron promoters to provide electrons to the d empty orbitals of iron or other metals, which can effectively promote the adsorption of CO_2 and suppress the adsorption of hydrogen, thereby reducing the production of methane and benefiting the production of light olefins [21–23]. Except for choosing active metals, many studies have shown that through modulating metal dispersion and interaction, regulating the surface PH values and pore structure, support may affect the transition of the metal active phase, and then the catalyst reactivity and product selectivity [24–27]. The interaction between the metal and the traditional metal oxide is too strong, which would inhibit the reduction and carbonization of the metal [28,29]. Compared with oxides, carbon support with tunable structures, such as carbon nanotubes (CNT_S), carbon spheres (CS), and graphene, have attracted attention [30–32]. Carbon materials have good hydrothermal stability and hydrophobicity, and their interaction with metals is weak, which is helpful for metal dispersion and carburization. Recently, carbon materials doped with electron-rich N components were used in CO_2 hydrogenation reactions [33], the addition of which will change the catalyst structure and electron density to affect the adsorption of CO_2 on the surface [34–36].

In addition to common carbon materials, metal–organic framework materials (MOFs) consisting of inorganic metal ions and organic ligands, have attracted much attention. Recently, several studies reported MOFs as sacrificial templates or precursors to form porous carbon supports by pyrolysis [37–39]. This pyrolysis usually produces metals or metal oxides embedded in the carbon matrix depending on the specific atmosphere [40], which makes the metal difficult to sinter and thus enhances its thermodynamic stability [41]. Among various MOFs materials, ZIF-67 is a kind of zeolite-like imidazole metal–organic framework materials with Co icons as the connection point. Loading iron on ZIF-67 can form a good bimetallic synergy effect with cobalt, while ZIF-67 shows the superior performance as a carbon support precursor. Among them, the role of Co in the CO_2 hydrogenation reaction has not been fully clarified. It is generally believed that Co has a higher FTS reactivity. Zhong [42] found that cobalt carbide formed during the CO carburization process can produce light olefins with high selectivity (around 60%). Davis [43] found that Co_2C has RWGS activity, and alkali metals can effectively stabilize the Co_2C phase, while it also significantly reduce the selectivity of methane. Therefore, it is a good strategy for designing Fe–Co bimetallic catalysts. Satthawong [44] found that adding a small amount of Co to Fe can effectively increase the selectivity of C_2^+ hydrocarbons and inhibit methane production, and in later work they found [45] that the Fe–Co/ Al_2O_3 catalyst modified by K can effectively improve the formation of light olefins. Li [46] used electrospinning to synthesize Fe–Co–Zr polymetallic fibers, and found that the addition of cobalt metal can not only greatly improve the reactivity, but is also conducive to resistance to sintering by the bimetallic synergistic effect and promote the production of light olefins. Guo [47] found that a Fe–Co bimetallic catalyst supported on Y-type zeolite can effectively convert CO_2 to linear olefins. However, most of the current researches on iron-cobalt bimetallic catalysts for CO_2 hydrogenation were concentrated on oxide supports or pure metals, and few studies on carbon support for CO_2 hydrogenation, lacking understanding of the composition of metal phases and changes during the CO_2 hydrogenation process on carbon support. Therefore, how to construct a suitable active phase interface to obtain the best activity and light olefin selectivity is a huge challenge.

Here, we report a ZIF-67-derived sodium-promoted iron-cobalt bimetallic catalyst and explore the properties, such as the size, phase change, and CO₂ hydrogenation performance of the metal nanoparticles at different pyrolysis temperatures. This work better understands the interaction of iron and cobalt on the ZIF-67 derived carbon support, and presents a new thought for further regulating the structure of catalyst and the product composition during the CO₂ hydrogenation reaction.

2. Results

2.1. Physical and Chemical Properties of Catalyst

Table 1 displayed the elemental composition and physical properties of the synthesis samples. The catalyst element composition was shown in Table 1 under different pretreatment temperatures, of which the relative proportion of cobalt and iron remain at 2, and the metal content increased ascribing to the H/N loss in MOFs during the pyrolysis process. Figure S1 shows the TG and DTG curves of ZIF-67 impregnated with iron. The catalyst had four-step thermal decomposition behavior: The first weight loss around 120 °C was considered to be related to the loss of physically adsorbed water. The weight loss with increasing temperature to around 150–200 °C may be due to the release of residual molecules (dimethylimidazole or methanol) and gas from the activation site [48]. The slight decomposition at about 300 °C may be attributed to the loss of iron acetylacetone. On the other hand, due to the decomposition of the skeleton, ZIF-67 had a significant mass loss at 400–500 °C [49].

Table 1. The physical properties of the synthesis samples.

Catalyst	T ^a (°C)	Metal content (wt %) ^b			S _{BET}	S _{micro}	S _{meso}	V _{micro}	V _{meso}
		Fe	Co	Fe/Co	(m ² g ⁻¹)	(m ² g ⁻¹)	(m ² g ⁻¹)	(cm ⁻³ g ⁻¹)	(cm ⁻³ g ⁻¹)
FeCo/NC	400	12.67	24.02	0.53	507	454	52.8	0.207	0.068
	500	18.13	34.89	0.52	61.0	0	61.6	0	0.137
	600	19.21	36.24	0.53	36.4	0	40.8	0	0.086
	700	20.60	40.0	0.52	72.9	0	74.9	0	0.124
ZIF-67	-	-	-	-	1318	1265	53.6	0.578	0.043

(a: Pyrolysis temperature; b: Measured by inductively coupled plasma (ICP)-OES).

The nitrogen adsorption–desorption isotherms of FeCo/NC-T are shown in Figure 1 and Table 1 to detect the structural properties. According to IUPAC classification, ZIF-67 shows a sharp N₂ uptake at a lower relative pressure (<0.05), suggesting that ZIF-67 has a good microporous structure [50]. However, FeCo/NC-T displays a type IV isotherm with the H3 hysteresis loop. The hysteresis loops caused by the capillary condensation closed at P/P⁰ ≈ 0.4, demonstrating the generation of mesopores [51]. The pore structure of ZIF-67 was gradually destroyed due to the raise of pyrolysis temperature, and part of the specific surface area sacrificed. Due to incomplete pyrolysis at 400 °C, part of the skeletal structure was retained, and the specific surface area of micropores decreased from 1265 to 454 m²g⁻¹. As the temperature further increased, the micropores of support gradually disappeared, and part of the micropores were transformed into mesopores [52].

The morphology and structure of prepared ZIF-67 and its derivatives by SEM are shown in Figure 2. ZIF-67 shows a typical rhombic dodecahedron shape (Figure 2a). As the pyrolysis temperature increased, the original structure of ZIF-67 was damaged, the particle surface became very rough and the boundary of the particle interface became blurred. Some self-grown carbon nanotubes were detected when temperature reached above 500 °C as shown in Figure 2b,d–f, which may be related to the catalytic growth induced by iron [53–55].

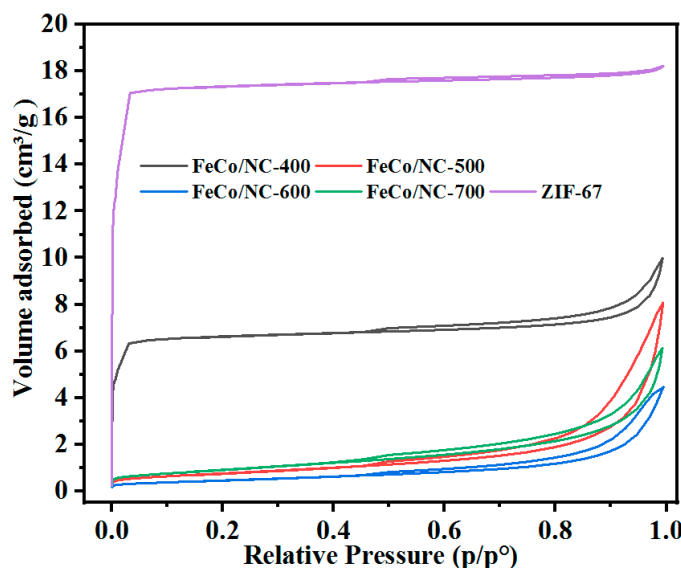


Figure 1. N_2 adsorption–desorption isotherms of FeCo/NC-T samples.

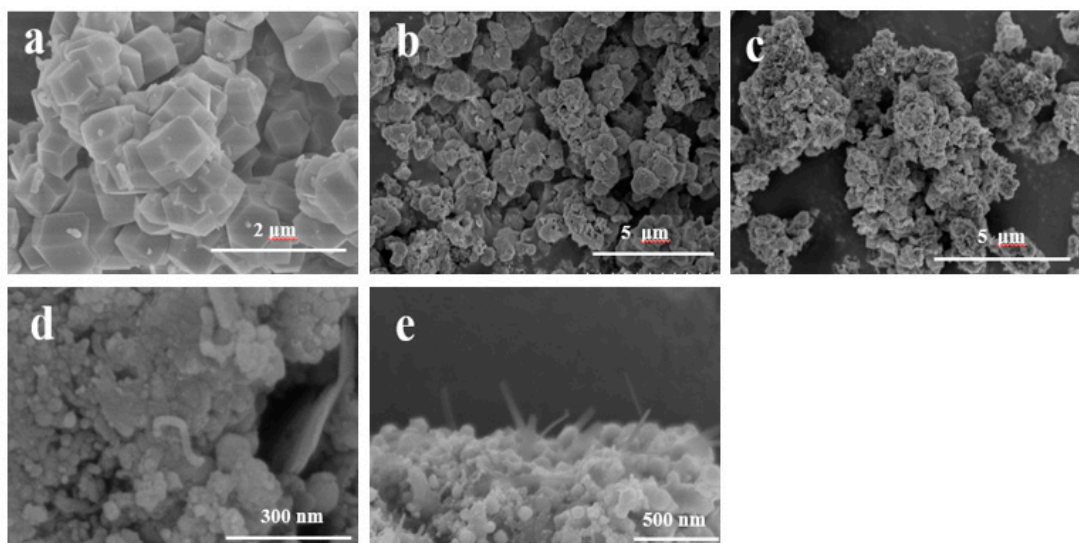


Figure 2. SEM images of (a) ZIF-67; (b) FeCo/NC-400; (c) FeCo/NC-500; (d) FeCo/NC-600; and (e) FeCo/NC-700.

XRD patterns of FeCo/NC-T are displayed in Figure 3. FeCo/NC-400 shows characteristic diffraction peaks ascribing to the reserved ZIF-67 framework structure at such temperature. Peaks at 30.08° , 35.43° , 43.06° , 56.94° , and 62.53° were attributed to the CoFe_2O_4 crystal phase (JCPDS no. 79-1744). When pyrolysis temperature reached above 500°C , the support skeleton completely collapsed, and only a peak of 44.86° was observed, which was assigned to the Fe–Co alloy phase (JCPDS no. 49-1567). With the raise of pyrolysis temperature, the intensity of the Fe–Co alloy diffraction peaks increased, and the FeCo/NC-700 demonstrated the best crystallinity.

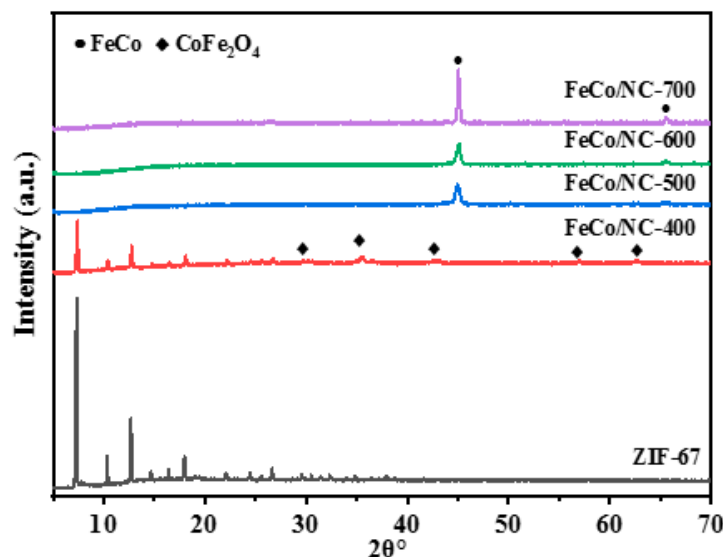


Figure 3. XRD images of fresh FeCo/NC-T catalysts.

The TEM result is shown in Figure 4 and Figure S2. On one hand, with the rise of pyrolysis temperature, the average particle size of the metal increased. The average particle diameters of FeCo/NC-400 to FeCo/NC-700 were 9.9 nm, 12.9 nm, 14.9 nm, and 40.8 nm, respectively (Figure S2a–d). Metal agglomeration became obvious when the pyrolysis temperature reached 700 °C. Moreover, pyrolysis at high temperature exposed more cobalt nanoparticles, which promoted formation of iron-cobalt alloys. On the other hand, it can be found from Figure 4 that as the temperature reached above 500 °C, a small amount of carbon nanotubes with a thickness of ca. 8–12 nm formed on the support (Figure 4b–d). Except for the metal nanoparticles distributed on the outer surface of the support, some metals are encapsulated in the mouth of the carbon nanotubes [56].

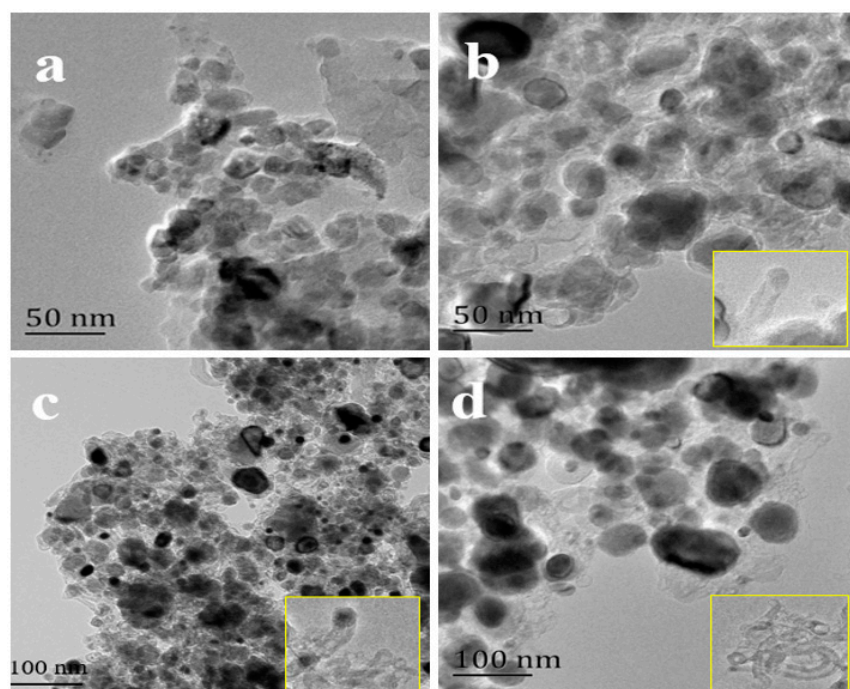


Figure 4. TEM images of: (a) FeCo/NC-400; (b) FeCo/NC-500; (c) FeCo/NC-600; and (d) FeCo/NC-700.

The structure of the catalyst was further studied by HRTEM, which is shown in Figure 5. When pyrolyzed at 400 °C (Figure 5a), the measured lattice fringes were 0.201 nm, 0.242 nm, and 0.484 nm, which corresponded to the crystal plane of FeCo (110), CoFe₂O₄ (006), and CoFe₂O₄ (003), respectively. When the temperature reached above 500 °C, only the FeCo (110) crystal plane could be found (Figure 5b), which might be attributed to the gas evolution with oxygen atoms during the decomposition of the ligand or the unstable decomposition of the oxide. In addition, the metal nanoparticles produced by MOFs carbonization were wrapped with graphitized carbon, which could effectively protect metal from sintering. However, when the pyrolysis temperature reaches 700 °C, the metal will obviously agglomerate without being protected by carbon [57].

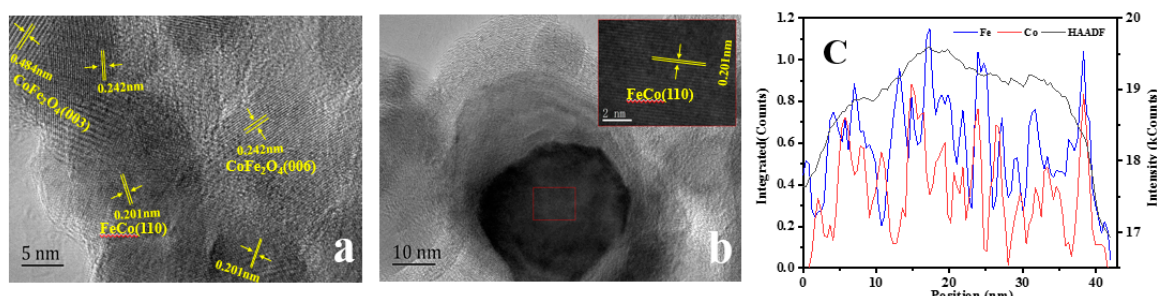


Figure 5. HR-TEM images of (a) FeCo/NC-400; (b) FeCo/NC-600; and (c) EDX spectra of FeCo/NC-600.

To observe the distribution of element species in detail, high angle annular dark field scanning transmission electron microscopy (HAADF-STEM) and EDS element mapping was used to analyze FeCo/NC-600. The metal nanoparticles (NPs) were relatively uniformly dispersed on the support (Figure 6b–d). The results show that in the particles of stem marked with a green line (Figure 6a), distribution position of Fe element was almost identical with that of Co element, but the Fe-rich position deviated from the Co-rich position in the NPs (Figure 5c). This result further proved the existence of FeCo alloy, which was corresponded to the XRD results.

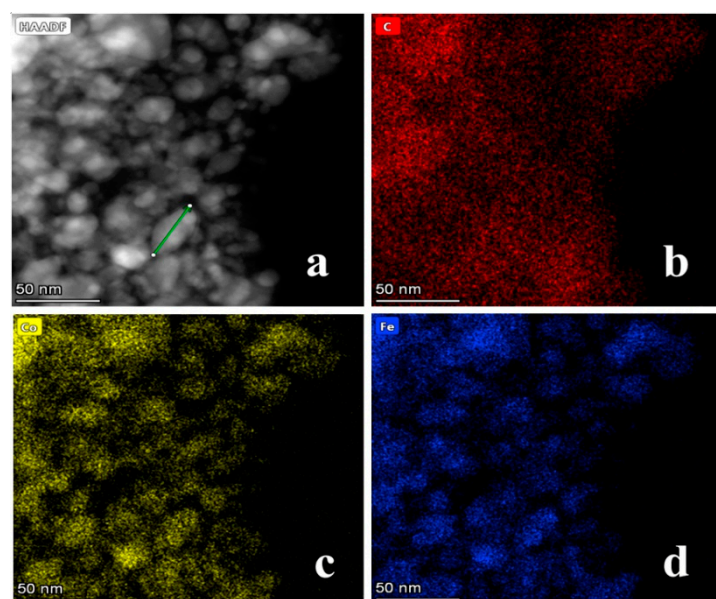


Figure 6. (a) High angle annular dark field scanning transmission electron microscopy (HAADF-STEM) images FeCo/NC-600 and (b–d) EDS mapping images of C, Co, and Fe.

To study the relationship between the degree of graphitization and the calcination temperature, FeCo/NC-T was analyzed by Raman spectra as displayed in Figure 7a. The D-band at 1345 cm⁻¹ and

the G-band at 1580 cm^{-1} were observed, attributed to disordered carbon and graphitic carbon [58]. The intensity proportion of the D-band to the G-band (I_D/I_G) shows the degree of graphitization of the carbon material. With the increasing of pyrolysis temperature, I_D/I_G decreased from 1.04 to 0.89, indicating that the graphitization degree became larger. In addition, the peak around 1425 cm^{-1} at $400\text{ }^\circ\text{C}$ could be attributed to the N = N stretching vibration during the formation of the C–N = N bond [37].

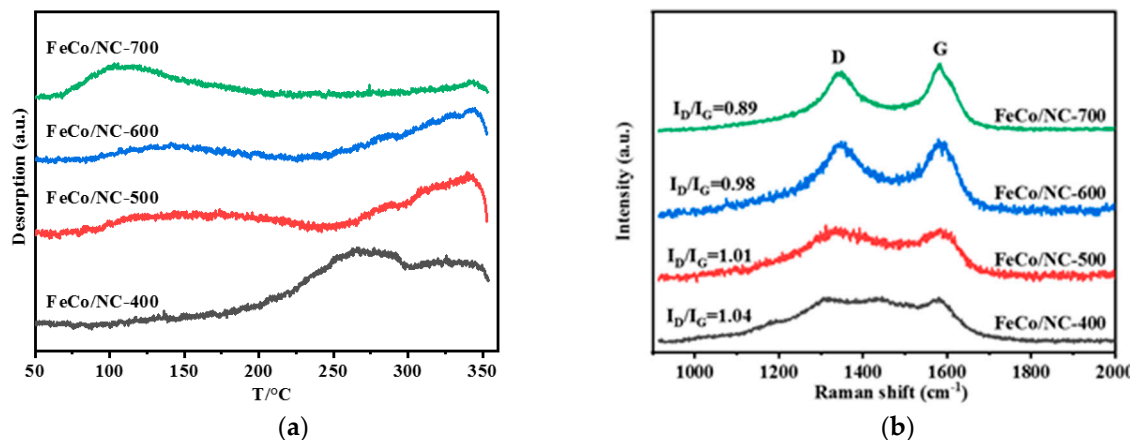


Figure 7. (a) Raman spectra of FeCo/NC-T catalysts and (b) CO₂-TPD of FeCo/NC-T catalysts.

To explore the basicity of the catalyst surface and the amount of CO₂ adsorbed, we used the CO₂-TPD method on the FeCo/NC-T catalyst (Figure 7b). In the test temperature range, three kinds of desorption peaks of 120 °C, 270 °C, and 350 °C were mainly observed. Among them, peaks around 120 °C comes from the weakly adsorbed alkaline sites, and the peaks at 270 °C and 350 °C correspond to the alkaline sites of medium intensity chemisorption [33,59]. It can be seen that with the raise of pyrolysis temperature, the adsorption of medium intensity became less and the weak physical adsorption increased. Table S1 shows the amount of adsorbed CO₂. With the rise of pyrolysis temperature, the quantity of CO₂ adsorbed on the surface decreased. More adsorption of CO₂ would contribute to higher CO₂ conversion.

XPS spectra were taken to study the chemical composition of nitrogen on the catalyst surface (Figure 8). The high-resolution N 1s spectra could be divided into three subpeaks at 398.5, 400.5, and 401.1, which belonged to the three N species of pyridinic N, pyrrolic N, and graphitic N (Figure 8a–d). The quantity of three N species was evaluated by fitting the area to the N 1s curve. The results show that with the rise of pyrolysis temperature, the total N content and pyridine nitrogen content decrease, and the graphite nitrogen content increased (Figure 8e) [35,60].

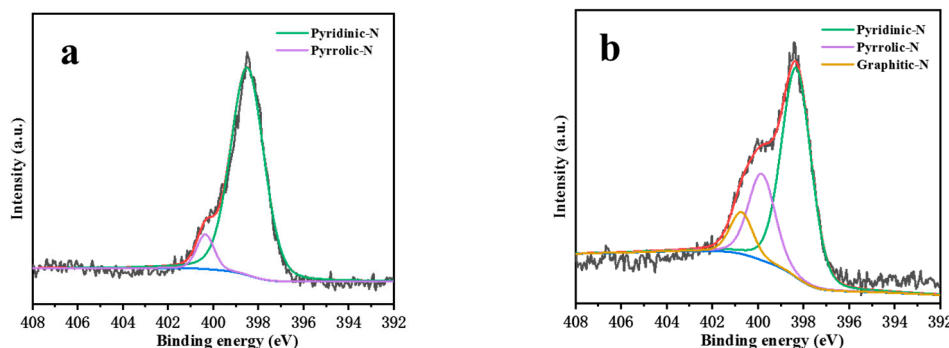


Figure 8. Cont.

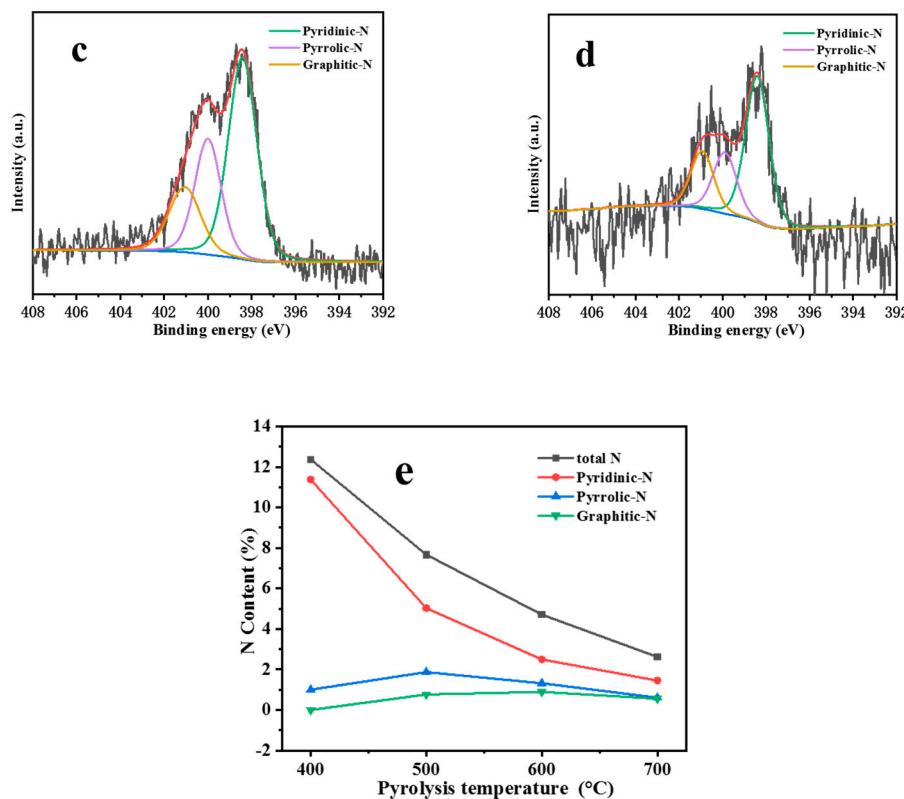


Figure 8. XPS analysis N 1s region of FeCo/NC-T catalysts (a) FeCo/NC-400; (b) FeCo/NC-500; (c) FeCo/NC-600; (d) FeCo/NC-700; and (e) N types and contents of catalysts.

The lower pyrolysis temperature led to a very low degree of graphitization of the support NC layer, and no graphitic nitrogen was found in FeCo/NC-400 (Figure 8a). As the temperature reached above 500 °C, the graphitization degree of the support increased and a small amount of graphitic nitrogen began to form (Figure 8b–d) [61]. The presence of nitrogen can provide anchor sites, which promotes high dispersion of the metal [40]. Pyridine-N would regulate the surface electron density and match the active metal, and then affect the CO₂ activity [62].

2.2. Activity Test

Table 2 summarizes the relationship between CO₂ conversion and product selectivity under a prepared catalyst during 32 h on stream. Additionally, FeCo/Al₂O₃ was evaluated as a comparison. The CO₂ conversion under FeCo/NC-400 and FeCo/NC-500 were 48.37% and 47.45%, which were higher than that of FeCo/NC-600 (37.03%) and FeCo/NC-700 (35.89%). FeCo/NC-400 shows the highest activity, ascribing to enhanced adsorbed CO₂ detected from CO₂-TPD. The turnover frequency (TOF) value of the FeCo/NC-T catalyst decreased with the increase of the pyrolysis temperature, which is the same change trend as the CO₂ conversion. It shows that after eliminating the influence of metal content, pyrolysis under low temperature conditions will facilitate the formation of iron oxides, thereby providing higher RWGS activity.

In addition, Pyridine-N can benefit the electron transfer of the catalyst and provide more anchor points for the metal active phase. XPS analysis of FeCo/NC-400 demonstrated the highest content of pyridine-N. Moreover, the smaller particle size of FeCo/NC-400 was helpful to more exposed active sites. The connection of Fe and O facilitated the Fe₃O₄ formation, which acts as the RWGS active phase. The result is shown in Mössbauer spectra as follows.

Table 2. CO₂ hydrocarbon conversion and product selectivity over the FeCo/NC-T catalysts.

Catalyst	CO ₂ conv. (%)	TOF (h ⁻¹)	Product Sel (C-mol%)				O/P ^a	
			CO	CH ₄	C ₂ –C ₄	C ₂ = – C ₄ =	C ₅ ⁺	alcohol
FeCo/NC-400	48.37	10.75	1.39	67.31	14.12	11.14	0.86	5.19
FeCo/NC-500	47.45	7.37	0.00	57.88	15.52	19.15	1.04	6.41
FeCo/NC-600	37.03	5.43	1.13	44.50	20.75	27.05	1.63	4.95
FeCo/NC-700	35.89	4.91	0.00	47.40	15.21	25.65	1.22	10.52
FeCo/Al ₂ O ₃	48.58	7.82	0.27	76.19	22.62	0.02	0.30	0.50

(a) Olefin to paraffin proportion (O/P) of C₂–C₄ over the FeCo/NC-T catalysts (reaction conditions: 0.50 g catalyst, 320 °C, 2 MPa, H₂/CO₂ = 3, space velocity = 6240 mL h⁻¹gcat⁻¹, and TOS = 32 h).

Mössbauer spectra are taken to identify the iron phases of the catalysts. The ⁵⁷Fe Mössbauer spectra of the FeCo/NC-600 catalyst are presented in Figure 9. The hyperfine parameters including central shift (CS), quadrupole splitting (QS), and hyperfine magnetic field (H) are shown in Table S2 and Figure S3. The spectrum (Figure 9a) consisted of one magnetic sextet with one central paramagnetic doublet. Stanfield and Delgass found [63] the hyperfine magnetic field within the range of 330–360 kOe (330 kOe for α-Fe). Hereby, the dominating sextet with parameters CS ~ 0.013 mm/s and H ~ 339.5 kOe was attributed to the α-(Fe,Co) alloy phase. The presence of the doublet could be due to the superparamagnetic (SP) effect of very small α-(Fe,Co) alloy particles (<10 nm), revealing the wide size distribution of metal particles. The after-reaction spectrum (Figure 9b) shows complex features with one doublet and six magnetic sextets, which can be assigned to iron oxides (FeOx) [64], α-(Fe,Co) alloy, and iron carbide (FeCx) [65] as listed in Table S2. The SP doublets in all after-reaction spectra had similar hyperfine parameters (CS ~ 0.27–0.30 mm/s, QS ~ 0.70–0.81 mm/s), which were ascribed to the ferric ions (Fe³⁺) from the FeOx phase. Gnanamani reported [66] that the doublet appearing in the room-temperature spectrum was resolved into a magnetite phase at 20 K. Herein, even though without low-temperature Mössbauer spectra, the SP doublet of FeOx phase could be inferred, because the sextet of magnetite phase disappeared in the Mössbauer spectrum of the FeCo/NC-700 catalyst. The mole fraction of FeCo, FeOx, and FeCx phases in various catalysts after reaction is shown in Figure 9c. With the rise of pyrolysis temperature, the content of Fe₅C₂ increased from 17% (FeCo/NC-400) to 55% (FeCo/NC-700). Correspondingly, the content of Fe₃O₄ decreased from 44% to 27%.

Methane selectivity under FeCo/NC-600 (44.50%) and FeCo/NC-700(47.40%) were significantly lower than that under FeCo/NC-400 (67.31%) and FeCo/NC-500 (57.88%). Relatively, the selectivity of C₂= – C₄= shows an upward trend, from the lowest 11.14% (FeCo/NC-400) to the highest 27.05% (FeCo/NC-600). The result shows that with the rise of pyrolysis temperature, the CO₂ conversion and CH₄ selectivity decreased, but the selectivity of light olefins increased. Higher pyrolysis temperature promoted the production of iron carbides in the reaction, which was detected from Mössbauer spectroscopy. These iron carbides are beneficial to the production of olefins and inhibit methane production. At the same time, the decrease in the content of Fe₃O₄ may result in a decrease in the activity of the RWGS reaction, which affects the conversion of CO₂. However, when the pyrolysis temperature reached 700 °C, the metal carbide active sites exposed decreased due to obvious agglomeration, therefore FeCo/NC-600 exhibited the highest selectivity for low olefins (27.05%). In addition, the C₂–C₄ olefins to paraffins ratio (O/P) of the product rise with increasing pyrolysis temperature, and FeCo/NC-700 shows the highest O/P (1.69). The decrease in the selectivity of C₂–C₄ paraffins at 700 °C might be attributed to the decrease in active sites that hinder the readsorption of light olefins and subsequent chain growth processes, which led to an increase in the value of O/P. The basic characterization of the FeCo/Al₂O₃ catalyst was added to the supporting materials (Figure S6 and Table S3), including XRD, BET, inductively coupled plasma (ICP), SEM, etc. It can be seen from BET that FeCo/Al₂O₃ had a sharp N₂ absorption at a lower pressure and a H1 hysteresis loop, indicating the presence of micropores and mesopores. The proportion of iron and cobalt obtained by ICP was consistent with FeCo/NC, which ensures similar reaction conditions. While, the result of SEM shows that the FeCo/Al₂O₃ still retained a relatively good morphology when calcined at 600 °C. It can be seen

from the XRD that iron and cobalt existed in the form of M_3O_4 ($M = Fe, Co$) on Al_2O_3 . The characteristic diffraction peaks of these two oxides were close to indistinguishable (Fe_3O_4 JCPDS no. 26-1136 and Co_3O_4 JCPDS no. 80-1541), but they did not form an alloy phase like $FeCo/NC$, so the synergy of bimetals was not obvious. At the same time, the strong interaction between the Al_2O_3 support and the metal was not conducive to the formation and stability of metal carbides. Therefore, although the $FeCo/Al_2O_3$ catalyst had a high RWGS activity, it lacked the active site for generating and stabilizing olefins, resulting in undesirable methane and C_2-C_4 paraffins with high selectivity.

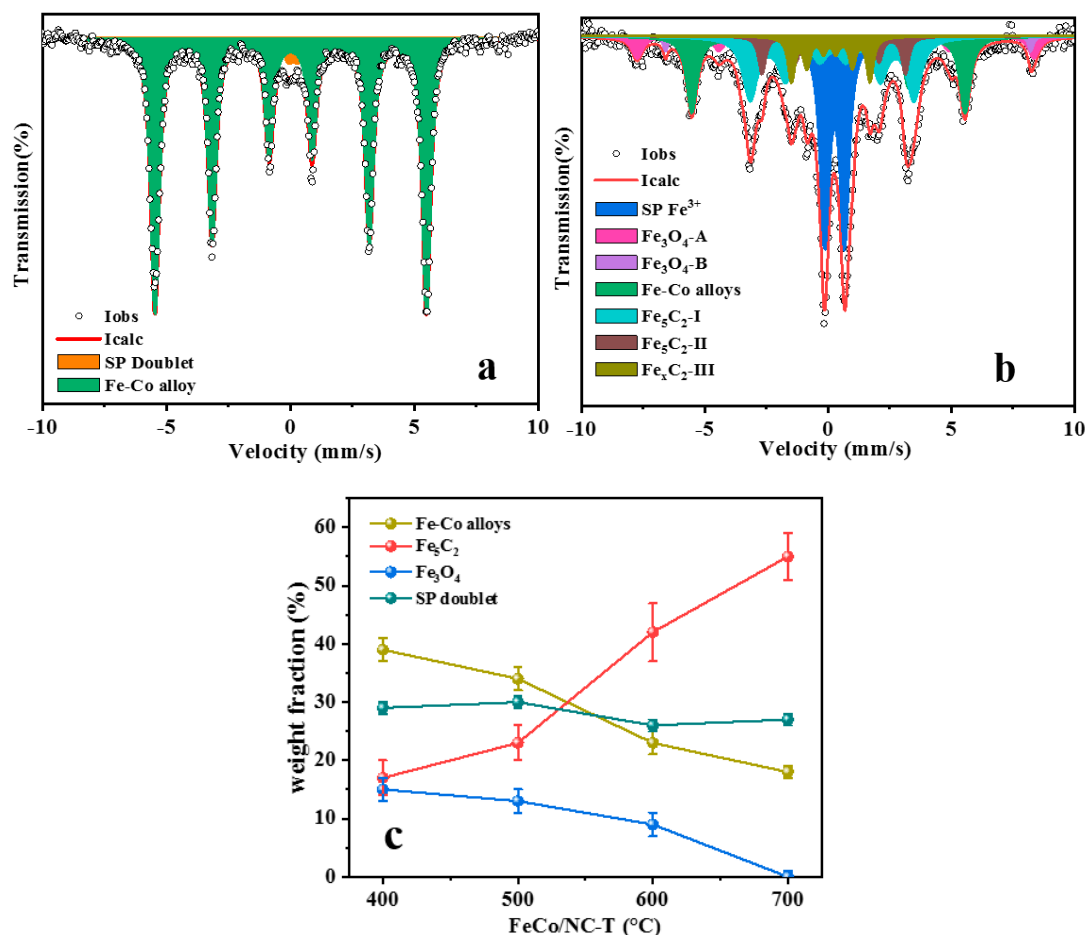


Figure 9. ^{57}Fe Mössbauer spectra of $FeCo/NC-600$ catalysts tested at room temperature before (a) and after (b) reaction and (c) the variations of different iron phases content in spent catalysts as a series of pyrolysis temperatures.

CO is a key factor for the reaction. Compared with a single iron, the addition of cobalt can effectively promote the conversion of CO. In the FTS process, the formation of alloy between cobalt and iron is beneficial to promote the oxidation and carburization of iron in the reaction. On the other hand, cobalt serves as the active site of FTS and formed the Co_2C phase during the reaction, which would promote light olefin production. The addition of sodium could effectively stabilize the presence of the Co_2C phase, as mentioned above. The metal Co will also generate some methane in the reaction, although the selectivity of methane has significantly decreased compared to the oxide support, from 76.19% to 44.50% ($FeCo/NC-600$). However, methane selectivity is still higher than expected due to the higher cobalt content in the support. To further regulate the active phase interface for better light olefin selectivity, it is important to properly control the metal content and the proportion of bimetal.

The XRD and HR-TEM results of the spent catalyst are shown in Figure 10. It can be obviously seen that the change of metal phase compared with that before the reaction (Figure 10a), and many new phases are shown in the XRD spectrum compared with spectrum before reaction (Figure 3). Fe_3O_4

and Fe_5C_2 phases could be observed, which are important active sites in the RWGS and FTS processes. In addition, the generation of Co_2C phase was also observed, which is believed to be beneficial to the production of olefins in the FTS reaction [42]. The HR-TEM images are shown in Figure 10b. The stripes with a lattice spacing of 0.280 nm measured on the spent $\text{FeCo}/\text{NC}-600$ catalyst correspond to the crystal plane of Fe_5C_2 (021). This is because the CO intermediate formed during the reaction promotes the carburizing process of Fe. The phase transformation of iron is corresponding to the previous results of Mössbauer spectroscopy.

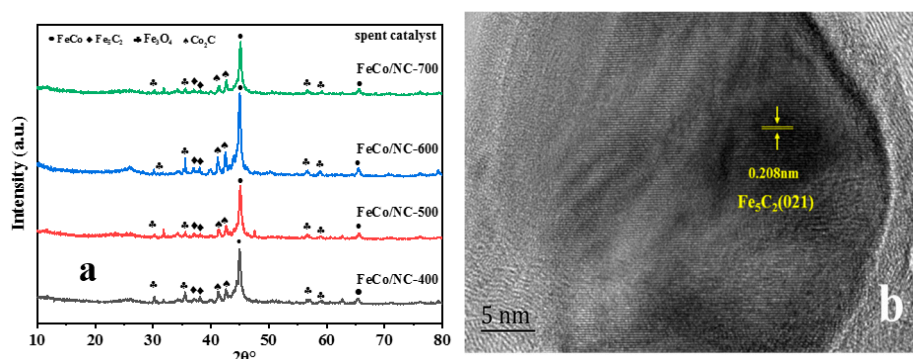


Figure 10. (a) XRD of spent $\text{FeCo}/\text{NC}-\text{T}$ catalysts and (b) HR-TEM images of spent $\text{FeCo}/\text{NC}-600$.

3. Materials and Methods

3.1. Catalysis Preparation

3.1.1. Preparation of Fe/ZIF-67

Fe/ZIF-67 catalysts were synthesized by traditional method of incipient wetness impregnation (IWI). Commonly, 0.2 g iron acetylacetone was dissolved in 1.8 mL methanol. Subsequently, it was added to the surface of 1 g ZIF-67 sample with stirring. The obtained product was dried at 25 °C for 8 h and at 110 °C overnight, and the impregnation behavior was repeated five times. NaNO_3 aqueous solution (0.136 g of NaNO_3 dissolved in 1.5 g of water) was added to the sample obtained above, and the obtained product was dried at 25 °C for 8 h and dried at 110 °C overnight. The obtained sample was named Fe/ZIF-67.

3.1.2. Preparation of FeCo/NC

FeCo/NC was prepared by the pyrolysis of pre-synthesized Fe/ZIF-67. The sample was heated up to specific temperature in nitrogen atmosphere (40 mL min^{-1}) with a heating speed of 3 °C/min and held for 150 min, then cooled down to 25 °C. The obtained product was named as FeCo/NC-T.

3.1.3. Synthesis of FeCo/ Al_2O_3

In the same way as above, an aqueous solution of 1.94 g of $\text{Fe}(\text{NO}_3)_3$ and 3.74 g of $\text{Co}(\text{NO}_3)_2$ was respectively mingled in deionized water, then it was added to Al_2O_3 (1.5 g). Promoted with the same amount of sodium for comparison. Subsequently the product was heated up to 600 °C in N_2 atmosphere (40 mL min^{-1}) with a heating speed of 3 °C/min and held for 2 h, then cooling down to 30 °C. The obtained sample was named as FeCo/ Al_2O_3 .

3.2. Catalyst Characterization

The element content of the FeCo/NC catalyst was analyzed by an inductively coupled plasma (ICP, Optima 2100DV, PE, MA, USA), and the FeCo/NC samples need to be digested with a microwave before the test. X-ray diffraction (XRD, Bruker, Karlsruhe, Germany) of the samples were tested with a D8-Focus diffractometer at the scan speed of 8 °C /min from 5 to 80 °C by using $\text{Cu-K}\alpha$ (40 kV, 200 mA)

irradiation. Scanning electron microscopy (SEM, HITACHI, Tokyo, Japan) was tested on a Regulus 8100 (30 kV accelerating voltage). The high-resolution transmission electron microscopy (HRTEM, HITACHI, Tokyo, Japan) and scanning transmission electron microscopy (STEM) images were taken by using a Thermo Fischer Talos F200X microscope with mapping and energy dispersive spectroscopic (EDS, TFS, MA, USA) analysis. In order to eliminate the variables that may exist in the discussion, all the pyrolyzed samples were pretreated with H₂ before the test.

Thermogravimetric (TG, TA, DE, USA) analysis was taken by using a Q500A equipment. The result was obtained with a ramping speed of 8 °C/min from 20 to 780 °C under a N₂ atmosphere. ASAP-2020 physical adsorption instrument was used to test the catalyst pore structure and specific surface area.

The degree of graphitization of carbon support after pyrolysis was tested by Raman with an excitation source of 532 nm.

Use X-ray photoelectron spectroscopy (XPS, TFS, MA, USA) to identify the surface properties of FeCo/NC samples with a monochromatic Al Ka radiation on a Thermo Scientific K-Alpha+ spectrometer. The curves were corrected according to carbon 1s spectra at 284.8 eV.

The phases and contents of iron species were identified by Mössbauer spectra (MS-500, Wissel, Germany) at room temperature. α-Fe absorber and ⁵⁷Co(Rh) source (25 mCi) was used. The curves fittings were measured by Lorentzian multiplet analysis.

CO₂ temperature programmed desorption (CO₂-TPD) was taken by using an AMI-300 apparatus. The type and amount of alkalinity on the catalyst surface and the CO₂ adsorption capacity were tested by the change of CO₂ concentration with the peak temperature. Firstly, a catalyst of 60 mg was pretreated under 10% H₂/Ar (25 mL·min⁻¹) at 400 °C for 60 min. Subsequently, the temperature was cooled down to 40 °C under Ar atmosphere and stay for 20 min. The test was taken by injecting continuous pulses of CO₂ into the He flow. The result was collected from 50 to 350 °C at a ramping rate of 8 °C·min⁻¹ in a He flow.

H₂ temperature programmed reduction (H₂-TPR) was taken by using an AutoChem II 2920 apparatus to get the best pretreatment temperature. The detailed description is listed in supporting.

Karl Fisher titration method was used to analyze the water content of liquid products on an 870 KF Titrino plus instrument

3.3. Catalytic Performances

Typically, a fixed-bed reactor with a 10 mm inner diameter was taken to test the CO₂ hydrogenation performance. 0.5 g sample (20–30 mesh) mixed with 3.5 g quarta sands (20–30 mesh) was loaded. Before the test, the sample was pretreated in H₂ (400 °C, 40 mL min⁻¹) for 2 h. Subsequently, the reactor was cooled down to the 50 °C and the mixed gas with a H₂/CO₂/N₂ ratio of 69/23/8 (N₂ used as an internal standard) was led in the reaction still under 2.0 MPa and 350 °C, the space velocity = 6240 mL g⁻¹ h⁻¹.

The reaction result was evaluated by operating two gas chromatographs. CO₂, CO, N₂, and CH₄ were studied by using a GC Micro 490 with a TCD detector. While hydrocarbons and oxygenates were researched by using a GC 2010 with an FID detector.

CO₂ conversion was evaluated by carbon atom balance according to the Equation:

$$\text{CO}_2 \text{ conversion} = \frac{\text{CO}_{2\text{in}} - \text{CO}_{2\text{out}}}{\text{CO}_{2\text{in}}} \times 100\%$$

CO_{2 in} and CO_{2 out} mean the molar fraction of CO₂ at the inlet and outlet of the reactor.

CO and different hydrocarbon selectivity were given as follows:

$$\text{CO selectivity} = \frac{\text{CO}_{\text{out}}}{\text{CO}_{2\text{in}} - \text{CO}_{2\text{out}}} \times 100\%$$

$$C_i \text{ selectivity} = \frac{\text{Mole of } C_i \times i}{\sum_{i=1}^n \text{Mole of } C_i \times i} \times 100\%$$

4. Conclusions

ZIF-67 was pyrolyzed at different temperatures to synthesize a carbon-encapsulated Fe–Co bimetallic catalyst, and the surface properties were promoted by sodium. We used different characterization methods to characterize the catalyst and evaluate the CO₂ hydrogenation activity, then further clarified the synergy of bimetals and the effect of pyrolysis temperatures on the samples. Compared with the traditional oxide support, the formation of the NC layer can effectively anchor and disperse the metal nanoparticles, promoting the reduction and carburization of the metal during the reaction, thereby forming a higher olefin selectivity. On the other hand, different pyrolysis temperatures had a profound effect on the degree of carbonization of the support, metal loading, particle size, and degree of carburization during the reaction. When the pyrolysis temperature was above 500 °C, the ZIF-67 was completely pyrolyzed, and the metal nanoparticles were well embedded in the generated carbon support. With the raise of the pyrolysis temperature, the carburization of the metal during the reaction was facilitated. The Fe₃O₄ content of the iron phase during the reaction decreased from 44% (400 °C) to 27% (700 °C). Relatively, the Fe₅C₂ content increased from 17% (400 °C) to 55% (700 °C). Meanwhile, part of the metal cobalt was converted into Co₂C, which also promoted the conversion of CO to light olefin in the FTS reaction. When the pyrolysis temperature reached 700 °C, the active sites exposed decreased due to sintering. Therefore FeCo/NC-600 exhibited the highest selectivity for low olefins (27.05%). These results are important for the subsequent further adjustment of the catalyst structure and metal composition, as well as the understanding of strategies for the control of active phase transition products of CO₂ hydrogenation. Such catalysts are currently being studied in more detail.

Supplementary Materials: The following are available online at <http://www.mdpi.com/2073-4344/10/4/455/s1>, Figure S1: TG and DTG of Fe/ZIF-67, Figure S2: TEM particle size distribution images, Table S1: CO₂-TPD results of different samples, Table S2: Hyperfine parameters of catalysts, Figure S3: ⁵⁷Fe Mössbauer spectra recorded at room temperature, Figure S4: XPS spectra of FeCo/NC-600, Figure S5: H₂-TPR spectra of FeCo/NC-600, Table S3: The physical properties of FeCo/Al₂O₃ sample, Figure S6: The basic properties of FeCo/Al₂O₃ sample

Author Contributions: Conceptualization, Z.D., J.Z. and Y.T.; Data curation, Z.D.; Formal analysis, Z.D.; Funding acquisition, J.Z.; Investigation, Z.D.; Methodology, Z.D. and B.Z.; Project administration, J.Z.; Resources, B.Z.; Supervision, Y.W.; Validation, Z.D.; Writing—original draft, Z.D.; Writing—review and editing, Y.T. All authors have read and agreed to the published version of the manuscript.

Funding: This research was funded by SINOPEC Research Institute of Petroleum Process and the Science and Technology Research Project of Henan Province (No. 202102210048).

Acknowledgments: We thank the Analysis and Testing Center of Tianjin University for its help in the characterization of this work.

Conflicts of Interest: The authors declare no conflict of interest.

References

1. Centi, G.; Quadrelli, E.A.; Perathoner, S. Catalysis for CO₂ conversion: A key technology for rapid introduction of renewable energy in the value chain of chemical industries. *Energy Environ. Sci.* **2013**, *6*, 1711–1731. [[CrossRef](#)]
2. Song, C. Global challenges and strategies for control, conversion and utilization of CO₂ for sustainable development involving energy, catalysis, adsorption and chemical processing. *Catal. Today* **2006**, *115*, 2–32. [[CrossRef](#)]
3. Yang, H.; Zhang, C.; Gao, P.; Wang, H.; Li, X.; Zhong, L.; Wei, W.; Sun, Y. A review of the catalytic hydrogenation of carbon dioxide into value-added hydrocarbons. *Catal. Sci. Technol.* **2017**, *7*, 4580–4598. [[CrossRef](#)]

4. Kondratenko, E.V.; Mul, G.; Baltrusaitis, J.; Larrazábal, G.O.; Pérez-Ramírez, J. Status and perspectives of CO₂ conversion into fuels and chemicals by catalytic, photocatalytic and electrocatalytic processes. *Energy Environ. Sci.* **2013**, *6*, 3112–3135. [[CrossRef](#)]
5. Guo, L.; Sun, J.; Ji, X.; Wei, J.; Wen, Z.; Yao, R.; Xu, H.; Ge, Q. Directly converting carbon dioxide to linear α -olefins on bio-promoted catalysts. *Commun. Chem.* **2018**, *1*, 11. [[CrossRef](#)]
6. Gao, P.; Dang, S.; Li, S.; Bu, X.; Liu, Z.; Qiu, M.; Yang, C.; Wang, H.; Zhong, L.; Han, Y.; et al. Direct Production of Lower Olefins from CO₂ Conversion via Bifunctional Catalysis. *ACS Catal.* **2017**, *8*, 571–578. [[CrossRef](#)]
7. Liu, X.; Wang, M.; Zhou, C.; Zhou, W.; Cheng, K.; Kang, J.; Zhang, Q.; Deng, W.; Wang, Y. Selective transformation of carbon dioxide into lower olefins with a bifunctional catalyst composed of ZnGa₂O₄ and SAPO-34. *Chem. Commun.* **2018**, *54*, 140–143. [[CrossRef](#)]
8. Li, W.; Wang, H.; Jiang, X.; Zhu, J.; Liu, Z.; Guo, X.; Song, C. A short review of recent advances in CO₂ hydrogenation to hydrocarbons over heterogeneous catalysts. *RSC Adv.* **2018**, *8*, 7651–7669. [[CrossRef](#)]
9. Nie, X.; Wang, H.; Janik, M.J.; Chen, Y.; Guo, X.; Song, C. Mechanistic Insight into C–C Coupling over Fe–Cu Bimetallic Catalysts in CO₂ Hydrogenation. *J. Phys. Chem. C* **2017**, *121*, 13164–13174. [[CrossRef](#)]
10. Sengupta, S.; Jha, A.; Shende, P.; Maskara, R.; Das, A.K. Catalytic performance of Co and Ni doped Fe-based catalysts for the hydrogenation of CO₂ to CO via reverse water-gas shift reaction. *J. Environ. Chem. Eng.* **2019**, *7*, 102911. [[CrossRef](#)]
11. Visconti, C.G.; Martinelli, M.; Falbo, L.; Infantes-Molina, A.; Lietti, L.; Forzatti, P.; Iaquaniello, G.; Palo, E.; Picutti, B.; Brignoli, F. CO₂ hydrogenation to lower olefins on a high surface area K-promoted bulk Fe-catalyst. *Appl. Catal. B Environ.* **2017**, *200*, 530–542. [[CrossRef](#)]
12. Xie, C.; Chen, C.; Yu, Y.; Su, J.; Li, Y.; Somorjai, G.A.; Yang, P. Tandem Catalysis for CO₂ Hydrogenation to C₂–C₄ Hydrocarbons. *Nano Lett.* **2017**, *17*, 3798–3802. [[CrossRef](#)] [[PubMed](#)]
13. Muleja, A.A.; Gorimbo, J.; Masuku, C.M. Effect of Co-Feeding Inorganic and Organic Molecules in the Fe and Co Catalyzed Fischer–Tropsch Synthesis: A Review. *Catalysts* **2019**, *9*, 746. [[CrossRef](#)]
14. Liu, M.; Yi, Y.; Wang, L.; Guo, H.; Bogaerts, A. Hydrogenation of Carbon Dioxide to Value-Added Chemicals by Heterogeneous Catalysis and Plasma Catalysis. *Catalysts* **2019**, *9*, 275. [[CrossRef](#)]
15. Puga, A.V. On the nature of active phases and sites in CO and CO₂ hydrogenation catalysts. *Catal. Sci. Technol.* **2018**, *8*, 5681–5707. [[CrossRef](#)]
16. Yang, X.; Zhang, H.; Liu, Y.; Ning, W.; Han, W.; Liu, H.; Huo, C. Preparation of Iron Carbides Formed by Iron Oxalate Carburization for Fischer-Tropsch Synthesis. *Catalysts* **2019**, *9*, 347. [[CrossRef](#)]
17. Herranz, T.; Rojas, S.; Pérez-Alonso, F.J.; Ojeda, M.; Terreros, P.; Fierro, J.L.G. Hydrogenation of carbon oxides over promoted Fe–Mn catalysts prepared by the microemulsion methodology. *Appl. Catal. A Gen.* **2006**, *311*, 66–75. [[CrossRef](#)]
18. Wang, X.; Zhang, J.; Chen, J.; Ma, Q.; Fan, S.; Zhao, T.-S. Effect of preparation methods on the structure and catalytic performance of Fe–Zn/K catalysts for CO₂ hydrogenation to light olefins. *Chin. J. Chem. Eng.* **2018**, *26*, 761–767. [[CrossRef](#)]
19. Al-Dossary, M.; Ismail, A.A.; Fierro, J.L.G.; Bouzid, H.; Al-Sayari, S.A. Effect of Mn loading onto MnFeO nanocomposites for the CO₂ hydrogenation reaction. *Appl. Catal. B Environ.* **2015**, *165*, 651–660. [[CrossRef](#)]
20. Wang, W.; Jiang, X.; Wang, X.; Song, C. Fe–Cu Bimetallic Catalysts for Selective CO₂ Hydrogenation to Olefin-Rich C₂⁺ Hydrocarbons. *Ind. Eng. Chem. Res.* **2018**, *57*, 4535–4542. [[CrossRef](#)]
21. Wei, J.; Sun, J.; Wen, Z.; Fang, C.; Ge, Q.; Xu, H. New insights into the effect of sodium on Fe₃O₄-based nanocatalysts for CO₂ hydrogenation to light olefins. *Catal. Sci. Technol.* **2016**, *6*, 4786–4793. [[CrossRef](#)]
22. Zhang, J.; Lu, S.; Su, X.; Fan, S.; Ma, Q.; Zhao, T. Selective formation of light olefins from CO₂ hydrogenation over Fe–Zn–K catalysts. *J. CO₂ Util.* **2015**, *12*, 95–100. [[CrossRef](#)]
23. Li, S.; Krishnamoorthy, S.; Li, A.; Meitzner, G.D.; Iglesia, E. Promoted Iron-Based Catalysts for the Fischer–Tropsch Synthesis: Design, Synthesis, Site Densities, and Catalytic Properties. *J. Catal.* **2002**, *206*, 202–217. [[CrossRef](#)]
24. Jun, K.-W.; Lee, S.-J.; Kim, H. Support effects of the promoted and unpromoted iron catalysts in CO₂ hydrogenation. *Stud. Surf. Sci. Catal.* **1998**, *114*, 345–350.

25. Li, S.; Xu, Y.; Chen, Y.; Li, W.; Lin, L.; Li, M.; Deng, Y.; Wang, X.; Ge, B.; Yang, C.; et al. Tuning the Selectivity of Catalytic Carbon Dioxide Hydrogenation over Iridium/Cerium Oxide Catalysts with a Strong Metal-Support Interaction. *Angew. Chem. Int. Ed. Engl.* **2017**, *56*, 10761–10765. [[CrossRef](#)]
26. Numpilai, T.; Wittoon, T.; Chanlek, N.; Limphirat, W.; Bonura, G.; Chareonpanich, M.; Limtrakul, J. Structure-activity relationships of Fe-Co/K-Al₂O₃ catalysts calcined at different temperatures for CO₂ hydrogenation to light olefins. *Appl. Catal. A Gen.* **2017**, *547*, 219–229. [[CrossRef](#)]
27. Yoon, S.; Oh, K.; Liu, F.; Seo, J.H.; Somorjai, G.A.; Lee, J.H.; An, K. Specific Metal-Support Interactions between Nanoparticle Layers for Catalysts with Enhanced Methanol Oxidation Activity. *ACS Catal.* **2018**, *8*, 5391–5398. [[CrossRef](#)]
28. Larmier, K.; Chizallet, C.; Raybaud, P. Tuning the metal-support interaction by structural recognition of cobalt-based catalyst precursors. *Angew. Chem. Int. Ed. Engl.* **2015**, *54*, 6824–6827. [[CrossRef](#)]
29. Wan, H.; Wu, B.; Xiang, H.; Li, Y. Fischer-Tropsch Synthesis: Influence of Support Incorporation Manner on Metal Dispersion, Metal-Support Interaction, and Activities of Iron Catalysts. *ACS Catal.* **2012**, *2*, 1877–1883. [[CrossRef](#)]
30. Chew, L.M.; Kangvansura, P.; Ruland, H.; Schulte, H.J.; Somsen, C.; Xia, W.; Eggeler, G.; Worayingyong, A.; Muhler, M. Effect of nitrogen doping on the reducibility, activity and selectivity of carbon nanotube-supported iron catalysts applied in CO₂ hydrogenation. *Appl. Catal. A Gen.* **2014**, *482*, 163–170. [[CrossRef](#)]
31. Cheng, Y.; Lin, J.; Wu, T.; Wang, H.; Xie, S.; Pei, Y.; Yan, S.; Qiao, M.; Zong, B. Mg and K dual-decorated Fe-on-reduced graphene oxide for selective catalyzing CO hydrogenation to light olefins with mitigated CO₂ emission and enhanced activity. *Appl. Catal. B Environ.* **2016**, *204*, 475–485. [[CrossRef](#)]
32. Williamson, D.L.; Herdes, C.; Torrente, M.L.; Matthew, D.J.; Davide, M. N-Doped Fe@CNT for Combined RWGS/FT CO₂ Hydrogenation. *ACS Sustain. Chem. Eng.* **2019**, *7*, 7395–7402. [[CrossRef](#)]
33. Li, Y.; Cai, X.; Chen, S.; Zhang, H.; Zhang, K.H.L.; Hong, J.; Chen, B.; Kuo, D.-H.; Wang, W. Highly Dispersed Metal Carbide on ZIF-Derived Pyridinic-N-Doped Carbon for CO₂ Enrichment and Selective Hydrogenation. *ChemSusChem* **2018**, *11*, 1040–1047. [[CrossRef](#)] [[PubMed](#)]
34. Ramirez, A.; Gevers, L.; Bavykina, A.; Ould-Chikh, S.; Gascon, J. Metal Organic Framework-Derived Iron Catalysts for the Direct Hydrogenation of CO₂ to Short Chain Olefins. *ACS Catal.* **2018**, *8*, 9174–9182. [[CrossRef](#)]
35. Zheng, Y.; Cheng, P.; Xu, J.; Han, J.; Wang, D.; Hao, C.; Alanagh, H.R.; Long, C.; Shi, X.; Tang, Z. MOF-derived nitrogen-doped nanoporous carbon for electroreduction of CO₂ to CO: The calcining temperature effect and the mechanism. *Nanoscale* **2019**, *11*, 4911–4917. [[CrossRef](#)]
36. Hu, S.; Liu, M.; Ding, F.; Song, C.; Zhang, G.; Guo, X. Hydrothermally stable MOFs for CO₂ hydrogenation over iron-based catalyst to light olefins. *J. CO₂ Util.* **2016**, *15*, 89–95. [[CrossRef](#)]
37. Liu, J.; Sun, Y.; Jiang, X.; Zhang, A.; Song, C.; Guo, X. Pyrolyzing ZIF-8 to N-doped porous carbon facilitated by iron and potassium for CO₂ hydrogenation to value-added hydrocarbons. *J. CO₂ Util.* **2018**, *25*, 120–127. [[CrossRef](#)]
38. Liu, J.; Zhang, A.; Jiang, X.; Zhang, G.; Sun, Y.; Liu, M.; Ding, F.; Song, C.; Guo, X. Overcoating the Surface of Fe-Based Catalyst with ZnO and Nitrogen-Doped Carbon toward High Selectivity of Light Olefins in CO₂ Hydrogenation. *Ind. Eng. Chem. Res.* **2019**, *58*, 4017–4023. [[CrossRef](#)]
39. Liu, J.; Zhang, A.; Liu, M.; Hu, S.; Ding, F.; Song, C.; Guo, X. Fe-MOF-derived highly active catalysts for carbon dioxide hydrogenation to valuable hydrocarbons. *J. CO₂ Util.* **2017**, *21*, 100–107. [[CrossRef](#)]
40. Lu, X.; Liu, Y.; He, Y.; Kuhn, A.N.; Shih, P.C.; Sun, C.J.; Wen, X.; Shi, C.; Yang, H. Cobalt-Based Nonprecious Metal Catalysts Derived from Metal-Organic Frameworks for High-Rate Hydrogenation of Carbon Dioxide. *ACS Appl. Mater. Interfaces* **2019**, *11*, 27717–27726. [[CrossRef](#)]
41. Zhang, J.; An, B.; Hong, Y.; Meng, Y.; Hu, X.; Wang, C.; Lin, J.; Lin, W.; Wang, Y. Pyrolysis of metal-organic frameworks to hierarchical porous Cu/Zn-nanoparticle@carbon materials for efficient CO₂ hydrogenation. *Mater. Chem. Front.* **2017**, *1*, 2405–2409. [[CrossRef](#)]
42. Zhong, L.; Yu, F.; An, Y.; Zhao, Y.; Sun, Y.; Li, Z.; Lin, T.; Lin, Y.; Qi, X.; Dai, Y.; et al. Cobalt carbide nanoprisms for direct production of lower olefins from syngas. *Nature* **2016**, *538*, 84–87. [[CrossRef](#)]
43. Gnanamani, M.K.; Jacobs, G.; Keogh, R.A.; Shafer, W.D.; Sparks, D.E.; Hopps, S.D.; Thomas, G.A.; Davis, B.H. Fischer-Tropsch synthesis: Effect of pretreatment conditions of cobalt on activity and selectivity for hydrogenation of carbon dioxide. *Appl. Catal. A Gen.* **2015**, *499*, 39–46. [[CrossRef](#)]

44. Satthawong, R.; Koizumi, N.; Song, C.; Prasassarakich, P. Bimetallic Fe–Co catalysts for CO₂ hydrogenation to higher hydrocarbons. *J. CO₂ Util.* **2013**, *3*, 102–106. [CrossRef]
45. Satthawong, R.; Koizumi, N.; Song, C.; Prasassarakich, P. Light olefin synthesis from CO₂ hydrogenation over K-promoted Fe–Co bimetallic catalysts. *Catal. Today* **2015**, *251*, 34–40. [CrossRef]
46. Li, W.; Zhang, A.; Jiang, X.; Janik, M.J.; Qiu, J.; Liu, Z.; Guo, X.; Song, C. The anti-sintering catalysts: Fe–Co–Zr polymetallic fibers for CO₂ hydrogenation to C₂ = –C₄ = –rich hydrocarbons. *J. CO₂ Util.* **2018**, *23*, 219–225. [CrossRef]
47. Guo, L.; Cui, Y.; Li, H.; Fang, Y.; Prasert, R.; Wu, J.; Yang, G.; Yoneyama, Y.; Tsubaki, N. Selective formation of linear-alpha olefins (LAOs) by CO₂ hydrogenation over bimetallic Fe/Co-Y catalyst. *Catal. Commun.* **2019**, *130*, 105759. [CrossRef]
48. Zhang, Z.-H.; Zhang, J.-L.; Liu, J.-M.; Xiong, Z.-H.; Chen, X. Selective and Competitive Adsorption of Azo Dyes on the Metal–Organic Framework ZIF-67. *Water Air Soil Pollut.* **2016**, *227*, 471. [CrossRef]
49. Liang, C.; Zhang, X.; Feng, P.; Chai, H.; Huang, Y. ZIF-67 derived hollow cobalt sulfide as superior adsorbent for effective adsorption removal of ciprofloxacin antibiotics. *Chem. Eng. J.* **2018**, *344*, 95–104. [CrossRef]
50. Tang, J.; Salunkhe, R.R.; Liu, J.; Torad, N.L.; Imura, M.; Furukawa, S.; Yamauchi, Y. Thermal conversion of core-shell metal-organic frameworks: A new method for selectively functionalized nanoporous hybrid carbon. *J. Am. Chem. Soc.* **2015**, *137*, 1572–1580. [CrossRef]
51. Sun, X.; Olivos-Suarez, A.I.; Osadchii, D.; Romero, M.J.V.; Kapteijn, F.; Gascon, J. Single cobalt sites in mesoporous N-doped carbon matrix for selective catalytic hydrogenation of nitroarenes. *J. Catal.* **2018**, *357*, 20–28. [CrossRef]
52. Wang, L.; Wang, Z.; Xie, L.; Zhu, L.; Cao, X. ZIF-67-Derived N-Doped Co/C Nanocubes as High-Performance Anode Materials for Lithium-Ion Batteries. *ACS Appl. Mater. Interfaces* **2019**, *11*, 16619–16628. [CrossRef]
53. Unni, S.M.; Anilkumar, G.M.; Matsumoto, M.; Tamaki, T.; Imaicd, H.; Yamaguchi, T. Direct synthesis of a carbon nanotube interpenetrated doped porous carbon alloy as a durable Pt-free electrocatalyst for the oxygen reduction reaction in an alkaline medium. *Sustain. Energy Fuels* **2017**, *1*, 1449–1632. [CrossRef]
54. Li, Z.; Liang, X.; Gao, Q.; Zhang, H.; Xiao, H.; Xu, P.; Zhang, T.; Liu, Z. Fe, N co-doped carbonaceous hollow spheres with self-grown carbon nanotubes as a high performance binary electrocatalyst. *Carbon* **2019**, *154*, 466–477. [CrossRef]
55. Gao, L.; Meiling, X.; Jin, Z.; Liu, C.; Zhu, J.; Ge, J.; Xing, W. Correlating Fe source with Fe-N-C active site construction Guidance for rational design of high-performance ORR catalyst. *J. Energy Chem.* **2018**, *27*, 1668–1673. [CrossRef]
56. Zhang, E.; Xie, Y.; Ci, S.; Jia, J.; Cai, P.; Yi, L.; Wen, Z. Multifunctional high-activity and robust electrocatalyst derived from metal–organic frameworks. *J. Mater. Chem. A* **2016**, *4*, 17288–17298. [CrossRef]
57. Xu, D.; Zhang, D.; Zou, H.; Zhu, L.; Xue, M.; Fang, Q.; Qiu, S. Guidance from an in situ hot stage in TEM to synthesize magnetic metal nanoparticles from a MOF. *Chem. Commun.* **2016**, *52*, 10513–10516. [CrossRef]
58. Sun, X.; Suarez, O.A.I.; Arteta, O.L.; Rozhko, E.; Osadchii, D.; Anastasiya, B.; Kapteijn, F.; Gascon, J. Metal-Organic Framework Mediated CobaltNitrogen-Doped Carbon Hybrids as Efficient and Chemoselective Catalysts for the Hydrogenation of Nitroarenes. *ChemCatChem* **2017**, *9*, 1854–1862. [CrossRef]
59. Chen, Q.; Qian, W.; Zhang, H.; Ma, H.; Sun, Q.; Ying, W. Effect of Li promoter on FeMn/CNTs for light olefins from syngas. *Catal. Commun.* **2019**, *124*, 92–96. [CrossRef]
60. Zhang, H.; Hwang, S.; Wang, M.; Feng, Z.; Karakalos, S.; Luo, L.; Qiao, Z.; Xie, X.; Wang, C.; Su, D.; et al. Single Atomic Iron Catalysts for Oxygen Reduction in Acidic Media: Particle Size Control and Thermal Activation. *J. Am. Chem. Soc.* **2017**, *139*, 14143–14149. [CrossRef]
61. Yuan, M.; Long, Y.; Yang, J.; Hu, X.; Xu, D.; Zhu, Y.; Dong, Z. Biomass Sucrose-Derived Cobalt@Nitrogen-Doped Carbon for Catalytic Transfer Hydrogenation of Nitroarenes with Formic Acid. *ChemSusChem* **2018**, *11*, 4156–4165. [CrossRef]
62. Wu, J.; Wen, C.; Zou, X.; Jimenez, J.; Sun, J.; Xia, Y.; Fonseca Rodrigues, M.-T.; Vinod, S.; Zhong, J.; Chopra, N.; et al. Carbon Dioxide Hydrogenation over a Metal-Free Carbon-Based Catalyst. *ACS Catal.* **2017**, *7*, 4497–4503. [CrossRef]
63. Stanfield, R.M.; Delgass, W.N. Mössbauer Spectroscopy of Supported Fe–Co Alloy Catalysts for Fischer-Tropsch Synthesis. *J. Catal.* **1981**, *72*, 37–50. [CrossRef]
64. Lyubutin, I.S.; Lin, C.R.; Korzhetskiy, Y.V.; Dmitrieva, T.V.; Chiang, R.K. Mössbauer spectroscopy and magnetic properties of hematite/magnetite nanocomposites. *J. Appl. Phys.* **2009**, *106*, 034311. [CrossRef]

65. Lyu, S.; Liu, C.; Wang, G.; Zhang, Y.; Li, J.; Wang, L. Structural evolution of carbon in an Fe@C catalyst during the Fischer–Tropsch synthesis reaction. *Catal. Sci. Technol.* **2019**, *9*, 1013–1020. [[CrossRef](#)]
66. Gnanamani, M.K.; Jacobs, G.; Hamdeh, H.H.; Shafer, W.D.; Liu, F.; Hopps, S.D.; Thomas, G.A.; Davis, B.H. Hydrogenation of Carbon Dioxide over Co–Fe Bimetallic Catalysts. *ACS Catal.* **2016**, *6*, 913–927. [[CrossRef](#)]



© 2020 by the authors. Licensee MDPI, Basel, Switzerland. This article is an open access article distributed under the terms and conditions of the Creative Commons Attribution (CC BY) license (<http://creativecommons.org/licenses/by/4.0/>).